Report on uncertainties as used in data products

WP410 - Deliverable D4.5

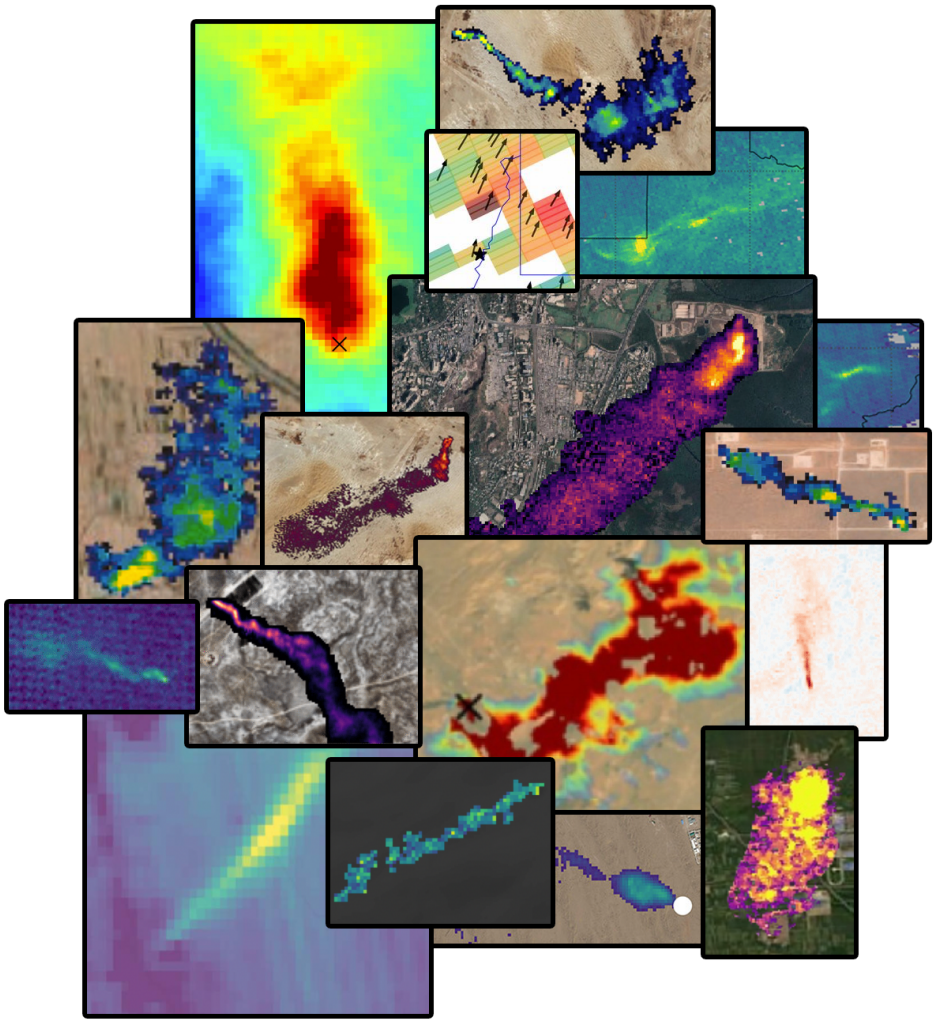

ESA Contract No. 4000143908/24/I-LR

Authors

Research Institute of Water and Environmental Engineering (IIAMA), Universitat Politècnica de València (UPV)

- Javier Gorroño (WP400 & document lead)
- Luis Guanter
- Javier Roger
- Shanyu Zhou

SRON Netherlands Institute for Space Research

- Joannes D (Bram) Maasakkers
- Matthieu Dogniaux
- Xin Zhang

Kayrros

- Julian Akani-Guery
- Alexis Groshenry

GHGSat Inc.

- Antoine Ramier

Institute of Environmental Physics, University of Bremen, Germany (IUP-UB)

- Michael Buchwitz

Approved by

Date: 2026-02-24 Signature: 	Date: Signature: 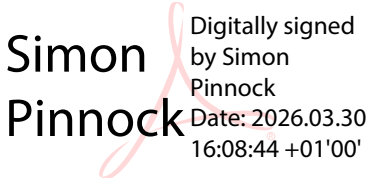
Ilse Aben (SRON) MEDUSA Science Lead	Simon Pinnock (ESA) Technical Officer

Change log

Version	Date	Status	Authors	Reason for change
0.1	17-September-2024	Draft	see Authors list	New document
1.0	4-April-2025	Draft	see Authors list	Version submitted to ESA
1.1	19-May-2025	Resubmitted to ESA	see Authors list	Revised based on RIDs received

Contents

1 Preface

This document corresponds to Deliverable 4.5 from Work Package (WP) 410, “Provision of uncertainties”, and Task 4.1, “Provision of uncertainties for data products used in Task 2 & Task 3”, of the *Methane Emissions Detection Using Satellites Assessment* (MEDUSA) project. It presents the current status of the methane flux rate uncertainty analysis from the different product providers participating in the validation and inter-comparison in Task 2 & Task 3. The report takes the current status of the uncertainty analysis to set a basis of potential activities and considerations towards a general and improved framework in Task 4.

The document is structured in three major sections following this preface. The first section reviews the literature on uncertainty reported with methane flux rates and discusses which are the main areas to improve in terms of uncertainty analysis; the second section details the current methodology for the reported methane flux rate uncertainty estimates. The third section contains a brief summary with major findings and potential improvements.

2 Literature review of methane flux rate uncertainty analysis

2.1 Methane retrieval uncertainty for plume mappers

The detection of methane plumes requires high-spatial resolution (typically below 100m) observations capable of defining the plume shape and attributing this to an emission source. Most of the retrieval of methane plumes employs the spectral region around 2.3 µm. Although these missions were not originally designed for methane detection , it is in this spectral region where absorption is broader and stronger Cusworth et al. (2019); Jongaramrungruang et al. (2021). The use of the 1.65 µm methane-absorption band with narrower and weaker absorption is challenging due to the need for tight spatial and spectral requirements. However, the radiance signal is higher, and some dedicated missions such as GHGsat can benefit from this spectral range.

The retrieval of methane concentration levels can be obtained with a full-physics retrieval such as the iterative maximum a posteriori differential optical absorption spectroscopy (IMAP-DOAS) algorithm (Frankenberg et al., 2005). This algorithm has been extensively applied to airborne missions, such as the Airborne Visible/Infrared Imaging Spectrometer (AVIRIS) (Thorpe et al., 2014; Borchardt et al., 2021). The retrieval isolates the local features from gas absorption from those features that are less prone to rapid variations such as surface reflectance and atmospheric scattering.

More recently, the matched-filter (MF) method has been widely implemented, because it is a faster method (as compared to a full-physics retrieval), directly retrieves the methaneenhancement and offers a superior performance with respect to other methodologies. This quantity can be directly applied for plume mapping and further emission quantification. The method has been

applied to different satellite missions such as EnMAP, PRISMA or EMIT (Thompson et al., 2016; Guanter et al., 2021; Irakulis-Loitxate et al., 2021). The matched-filter method fits the measured spectrum to a reference spectrum. This reference is generated from a statistical reference background spectrum from the image further convolved with the methane absorption spectrum (Thompson et al., 2015; Foote et al., 2020).

In the case of band imagers / multispectral imagers such as Sentinel-2/Landsat-8/9, both a temporal and spectral ratio of bands can be used as a proxy of methane enhancement transmission Varon et al. (2020). It assumes that the spectral bands are adjacent and that the different observations do not contain an overlaying plume. This transmission can be further associated with a methane enhancement estimate with a radiative transfer or a mathematical relationship such as Beer's law. MF methodologies can also be applied to multispectral methodologies (Wang et al., 2024). However, this methodology does not offer significant advantages in terms of performance if spectral channels are broad.

In general, for any methane retrieval methodology we can find the following main uncertainty contributions:

- Noise propagation
- Background level knowledge.
- Outliers and local artefacts.

The *Noise propagation* directly refers to the instrument noise propagated to the resulting methane enhancement map. On the one hand, the quantification of this effect can be measured directly on the resulting map independently of the mission and methodology Varon et al. (2021); Guanter et al. (2021); Sánchez-García et al. (2022). On the other hand, we can specify an analytical propagation of the noise based on the measurement equation as in Fahlen et al. (2024).

The former procedure is straightforward, but has the main drawback that the resulting error distribution accounts for both methane enhancement noise and scene and methane plume variations. Although efforts can be undertaken to minimise the scene impact (e.g. select an area with low artefacts), it will always be an overestimation of the expected noise. The latter method provides a bias-removed statistical uncertainty per-pixel but requires an explicit mathematical formulation that correctly captures the mathematical relationship, error correlations, and expected distribution. This is hard to model for some missions and retrieval methodologies where the mathematical relationship might not be fully explicit and assumptions such as nonlinear response or Gaussian distribution are included.

Based on the previous considerations, noise propagation schemes require a validation procedure that defines its domain of validity. The MonteCarlo (MC) is a well-suited reference since it requires no explicit mathematical model and fully propagates any input distribution to the output

considering internal dependencies. In our specific case, this also accounts for the spectral and spatial error correlations (JCGM, 2008; BIPM et al., 2011).

The *Background level knowledge* is not generally considered or introduced as part of any uncertainty budget and would require a dedicated study. For a band ratio, this is introduced by different biases in the temporal or spectral normalisation that are partly (or not) compensated. In the case of the MF, this is the consequence of assuming a global population for an entire image (or row) that might not be locally representative.

Finally, an important source of uncertainty is that associated with *outliers and local artefacts* that appear in the resulting methane enhancement as unexpected areas with significant low/high concentrations. Some of these effects can be compensated (e.g., vertical striping in data-driven methods by calculation per-column), flagged (e.g., cloud and cloud shadows), or minimised (e.g., consider a larger wavelength range as in Roger et al. (2024a)). Others, such as certain plastics, exhibit a strong absorption in the 2.3 µm band, that difficult to minimise during retrieval.

At the time of writing, there are no uncertainty estimates that consider the impact of outliers and local artefacts. In general, these are difficult to translate into an uncertainty value and other types of metrics seem more convenient. For example, a sensitivity metric as proposed in Fahlen et al. (2024) or a global statistical prediction could be considered.

2.2 Flux rate uncertainty for plume mappers

Once the $\Delta XCH4$ map has been obtained, the processing continues with the detection and emission quantification of methane plumes. Current methods rely on the mass-balance concept and associate the methane concentration enhancements with single point source emission rates.

The most widely used method for plume emission quantification with high-resolution satellite data is the integrated mass enhancement (IME) method, which was first introduced by Frankenberg et al. (2016) for aircraft measurements and was first applied to satellite data by Varon et al. (2018). For simplification reasons, this is the method selected here to describe the uncertainty of reported flux rates with concepts readily applicable to other methods such as the cross-sectional flux (CSF) method (Krings et al., 2011).

The method estimates the emission flux rate as the total mass enhancement in the plume scaled with a coefficient dependent on the wind speed. The IME in kg is defined as the total excess mass of methane contained in the plume,

$$\text{IME} = k \sum_{i=1}^{n_p} \Delta XCH4(i), \tag{2.1}$$

where n_p is the number of pixels in the plume and k is a scaling factor which converts the total of pixel-wise methane concentration values in ppb to kg by assuming Avogadro's law and taking

into account the pixel size (e.g., k =5.155·10^{-3} kg/ppb for 30 m pixel).

This total mass enhancement is scaled to obtain the flux rate Q as follows:

$$Q = \frac{U_{\text{eff}} \cdot \text{IME}}{L}, \tag{2.2}$$

where U_{eff} is an effective wind speed and L the plume length scale in m, which is typically approximated by the square root of the plume mask area.

Regarding U_{eff}, this term is intended to account for turbulent diffusion of the methane flux, and also for the fraction of the plume which is not detected due to retrieval noise (Varon et al., 2018). U_{eff} can be expressed as a linear or logarithmic function of the measurable 10-m wind speed U_{10} available from the reanalysis products. This function can be defined with modelled plume simulations thereby accounting for the corresponding spatial sampling and retrieval noise of each specific instrument. For example, the linear relationship displayed here as follows:

$$U_{\text{eff}} = 0.33 \cdot U_{10} + 0.45 \tag{2.3}$$

was derived using large-eddy simulations specifically performed for a spatial resolution and retrieval precision compatible with Sentinel-2 data by Varon et al. (2021).

Following expressions in 2.1, 2.2 and 2.3, we can identify a series of uncertainty sources that are expected to contribute to the flux rate uncertainty budget.

The uncertainty in IME has direct contributions from both k and $\Delta XCH4$. The former uncertainty contribution is not considered in current flux rate uncertainty estimates. It refers to a unit conversion in which the uncertainty of Avogadro Law and the molar mass of methane must be considered negligible. However, there is *limited knowledge of the spatial resolution* of the pixel that is typically defined by the point spread function (PSF) or modulation transfer function (MTF)(Markham, 1985). This limited knowledge can be attributed to pre-flight measurement uncertainty but also due to changes across the focal plane or thermolastic effects. The uncertainty for $\Delta XCH4$ is discussed in subsection 2.1. It is typically applied in the uncertainty budget as a representative value of a single pixel (Sánchez-García et al., 2022). However, when applied in the context of a methane emission quantification, it is expected that the combined value of $\Delta XCH4$ *plume mask uncertainty* is lower than the assigned at a pixel level due to the error spatial correlation.

The uncertainty associated with the L term in 2.2 is also not included in the available literature. This effect needs to be assessed in combination with the *limited knowledge of the spatial resolution* in k term since both terms are affected by the pixel spatial resolution.

The uncertainty associated with the U_{eff} in Eq. 2.3, can be subdivided into the *uncertainty in the* U_{eff} *calibration* and *the uncertainty in* U_{10}.

The first of them arises from the incomplete knowledge of the relationship between the flux

rate Q and IME. The calibration U_{eff} relies on simulated plumes that introduce systematic and random component errors Gorroño et al. (2023). These errors arise during the fitting between U_{eff} and U_{10} as a result of sensor noise, different plume shapes and the fitting method itself. These errors can range between 30 and the 75% error for different cases (Jervis et al., 2021; Varon et al., 2020). In addition to the error during the fitting process, the calibration U_{eff} is also sensitive to small variations in the parameterised simulation Sánchez-García et al. (2022) and is based on the accuracy of the simulations themselves. In some cases, such as in the AVIRIS mission, the U_{eff} can be directly modelled as U_{10} Thorpe et al. (2023).

In general, either the use of a calibrated U_{eff} or directly U_{10} requires a thorough validation. Technically, we need the 3D wind field convolved with the 3D methane plume. The effective wind speed is the vertically averaged wind speed weighted by the vertical profile of the trace gas concentration. Since we cannot get this for the exact time efforts must be directed towards an improved calibrated U_{eff} that relies on realistic and sophisticated simulation.

The formulation of the IME itself can be challenged with simulations that might become more realistic and consider aspects such as topography or realistic atmospheric setup such as in Hald et al. (2019) or even the 3D complexity of atmospheric propagation such as in Schwaerzel et al. (2020). We can better understand the *parameterisation sensitivity*, *representativeness of the calibration* and *fitting error* by leveraging these enhanced simulations. We must also understand the absolute accuracy of these simulations, hence the U_{eff} calibration, by comparing against controlled-releases such as in Conrad et al. (2023). This same study also illustrates an expected challenge: the quantification uncertainty is highly skewed. Therefore, reporting the flux rate will require the determination of the error distribution.

For the U_{10} term, an uncertainty of 2 m/s has been reported in Varon et al. (2018). This study compared local wind speed values measured at different airports with the GEOS-FP values. More recently, the study in Guanter et al. (2024) set a similar U_{10} uncertainty value of 2 m/s for values equal or greater than 4 m/s (50% relative error for values below the threshold) based on the validation of MERRA-2 products in Carvalho (2019). Other studies such as in Ayasse et al. (2024) estimate the wind uncertainty based on the spatial and temporal variability. In this case, it is based on the standard deviation from a 9 km window around the source location and from a 3 hour window around the plume acquisition.

These initial U_{10} uncertainty estimates prove critical to estimate a flux rate uncertainty budget since they are, in many cases, the dominant source of uncertainty. Due to the impact on the total uncertainty budget of U_{10}, it is also critical that further efforts are directed towards a better understanding of this uncertainty source. The U_{10} uncertainty budget can be decomposed into a U_{10} *product uncertainty* and a *representativeness of the spatiotemporal domain*.

The inclusion of U_{10} uncertainty as part of the operational products is the preferred approach since it streamlines the production of methane products. This is already (partially) occurring for ERA5 (Soci et al., 2024) and ERA5 Land products (Muñoz Sabater et al., 2021) which include a

10-member ensemble spread. However, the perturbations are typically an underestimation with mostly random components and not systematic ones. In addition, it does not consider the physics of surface model MacLeod et al. (2016). Therefore, it is critical that these products investigate further development of uncertainty sources (mostly surface) to provide realistic uncertainties to land reanalysis.

Connected with the importance of surface modelling is the concept of spatial representativeness. The small-scale domain of many methane emissions as compared to representativeness of most wind reanalysis products highlights the importance of considering this effect in detail. For example, the Global Wind Atlas presented in Davis et al. (2023) displays the wind climatology at 250 m spatial resolution. In terms of spatial representativeness, this downsampling suggest the importance of topographic effects to quantify this contribution. Furthermore, the temporal representativeness also needs to be considered and accounted for. The work in Conrad et al. (2023) showcases an example where the consideration of either *averaged* or *gust* products has an important impact over the expected flux rate error distribution.

2.3 Methane retrieval uncertainty for area mappers

The algorithm to estimate the operational XCH4 product from TROPOMI is detailed in Hu et al. (2016); Lorente et al. (2023). It is based on an inference of the atmospheric state vector x from TROPOMI spectral bands y in the NIR (757–774 nm) and SWIR (2305–2385 nm). The modelled measurement can be computed for an atmospheric state as follows:

$$y = F(x) + e_y + e_F \tag{2.4}$$

where F is the forward model, e_y is the measurement noise error, and e_F is the forward model error.

In order to retrieve the state vector the Eq. 2.4 must be inverted. This inversion finds a state vector at the minimum of the least-squares cost function and a weighted term constrained by the regularisation parameter γ following the expression:

$$\hat{x} = \min_x(\|S_y^{-1/2}(F(x) - y)\|^2 + \gamma\|W(x - x_a)\|^2) \tag{2.5}$$

where S_y is the diagonal measurement error covariance matrix, x_a is an a-priori state vector, and W is a diagonal weighting matrix that ensures that only the CH4 parameters and the scattering parameters contribute to its norm.

The operational level-2 TROPOMI methane product provides the standard deviation of the retrieval noise. This precision σ_{XCH4}, follows from the error covariance matrix S_x, which describes the noise mapping from the observation space into the retrieval according to Eq. 2.5. For appli-

cations requiring the full uncertainty, the level-2 product documentation advises users to multiply the provided error by a factor 2. TROPOMI methane data has extensively been validated against the Total Carbon Column Observing Network (TCCON). Lorente et al. (2023) report a mean bias of -0.3% (-5.3 ppb), a station-to-station variability of 0.3% (5.1 ppb), and station-wise single measurement precisions ranging between 0.5% (8.7 ppb) and 0.9% (17.3 ppb). The scatter of the single sounding errors in the TCCON validation is similar to the aforementioned provided uncertainty multiplied by a factor two.

The operational methane product includes a posterior albedo correction parametrized based on the assumption that the retrieved methane concentration must be constant over areas without sources with varying albedo. To further mitigate bias in the TROPOMI methane concentration maps, Balasus et al. (2023) developed an ensemble model that performs an additional posteriori correction of the TROPOMI XCH4 product. This correction is done to further (as much as possible) mitigate remaining retrievals biases related to for example surface albedo and aerosol scattering. The model leverages GOSAT's better spectral resolution, with its 1.6um channel and proxy retrieval approach, to correct the TROPOMI – GOSAT bias in TROPOMI data using only variables included in the TROPOMI level-2 product files. The largest corrections performed by this model are associated with coarse aerosol particles and high shortwave infrared albedo. Compared to reference methane XCH4 data from TCCON, the blended TROPOMI+GOSAT product shows a mean bias of 4.4 ppb and a single measurement precision of 11.9 ppb. However, the inclusion of a statistical model at the end of the processing chain complicates the calculation of XCH4 uncertainty.

Finally, another TROPOMI L2 Methane product is produced by the University of Bremen, using the Weighting Function Modified Differential Optical Absorption Spectroscopy algorithm (Schneising et al., 2019, 2023). Similarly to the operational product (albeit some differences in the forward and inverse approach choices), it fits the Methane total column by aiming to minimize the difference between simulated and observed spectra. Comparison of TROPOMI/WFMD results against TCCON shows a single-measurement precision of 12.4 ppb.

Further evaluation or improvement of the uncertainty in the TROPOMI level-2 product is not included in the MEDUSA project.

2.4 Flux rate uncertainty for area mappers

Following the generation of an XCH4 map, three steps still need to be completed for area mappers: methane plume detection, background subtraction, and emission quantification.

The detection (with segmentation) of methane plumes is – in the case of the SRON approach Schuit et al. (2023) - accomplished through machine learning techniques, which will be elaborated upon in Section 2.5.

Background removal can be performed either prior to detection (Lauvaux et al. (2022)) or

after detection (Schuit et al. (2023)). The approach of Schuit et al. (2023) requires a plume mask and defines the local background as the median value of the pixels of the scene external to the mask. In contrast, Lauvaux et al. (2022) aim to estimate the background before identifying methane plumes. Their method dynamically defines the background on an 11x11 pixel patch using the following equation.

$$background = \begin{cases} median, & \text{if } \frac{mean-median}{std} \geq 0.3 \\ l * (median) - (l-1) * mean & \text{otherwise} \end{cases} \tag{2.6}$$

where l is a hyperparameter optimized to minimize false detections while maximizing the identification of known hotspots. As described in Lauvaux et al. (2022), the methodology for background computation is of critical importance. To assess the associated uncertainty, they conducted a sensitivity analysis on a set of 200 randomly selected plumes. The influence of the background on the final result was evaluated by quantifying each plume using four different background removal techniques. The analysis led to an estimated relative uncertainty of 10%. Similarly, Schuit et al. (2023) employed an ensemble approach to quantify uncertainty. In their method, the background concentration is adjusted by ± 2 times the mean level-2 XCH4 uncertainty to account for potential variations in the background estimation.

Several methodologies exist in the literature for estimating source rates of plumes observed by area mappers. The Integrated Methane Enhancement (IME) method, originally developed for high-resolution instruments and described in section 2.2, is frequently applied to area mappers as well. The main distinction in its application to area mappers lies in the expression of the effective wind speed, U_{eff}. Schuit et al. (2023) calibrated U_{eff} by quantifying 15,336 plumes simulated using the Weather Research and Forecasting model coupled with a Chemistry module (WRF-Chem). Finding that the most representative wind can vary on a case-by-case basis, they incorporated three distinct wind measurement data sources: ERA-5 10m, GEOS-FP 10m, and GEOS-FP planetary boundary layer (PBL). Their analysis revealed that the dependence of U_{eff} on both the PBL wind U_{PBL} and U_{10} is more accurately described by a linear relationship.

$$U_{\text{eff}} = 0.47 * U_{\text{PBL}} + 0.31 \tag{2.7}$$

$$U_{\text{eff}} = 0.59 * U_{10} + 0.00 \tag{2.8}$$

They used the mean of the three resulting U_{eff} values (using two different U_{10} values) to quantify emissions. In their ensemble method approach, they vary for the mean U_{eff}:

- the wind values from -50% to +50%, with a step of 10%
- the coefficients in Eq. 2.7 and 2.8 from -5% and 5% with a step of 1%.

Another well-known approach used to quantify methane plumes for area mappers consists of fitting the XCH4 map with a physical simulation generated with an atmospheric transport model. Pandey et al. (2019) and Cusworth et al. (2021) use the Weather Research and Forecasting Chemistry (WRF-Chem) model in a model scaling approach, Maasakkers et al. (2023) use the same model for a Bayesian inversion to estimate emissions. Lauvaux et al. (2022) bases its quantification on the Lagrangian particle dispersion model HYSPLIT. The transport models uses weather data and rely on both the wind speed and the wind direction, compared to the IME method that uses only the wind speed.

2.5 Flux rate uncertainty and detection with machine learning methods for plume imagers

Estimating methane flux rates from satellite and airborne remote sensing data presents significant challenges due to uncertainties arising from atmospheric conditions, sensor limitations, and variations in plume dispersion dynamics. Traditional flux inversion techniques, such as the Integrated Mass Enhancement (IME), depend heavily on the accuracy of wind speed and direction to estimate emission rates. However, wind field information is typically derived from coarse-resolution weather models, such as ERA5 (9 km resolution) or GFS (28 km resolution), which can introduce substantial uncertainties, sometimes exceeding 50% (Roger et al., 2024b; Joyce et al., 2023; Guanter et al., 2021). These uncertainties arise not only from the spatial and temporal resolution mismatch between satellite observations and meteorological data but also from inherent variability in local wind conditions that are not captured by global models.

To address these limitations, machine learning (ML) methods have been increasingly employed for methane emission rate estimation, offering potential advantages in reducing the dependence on external wind data and leveraging spatial-spectral patterns in remote sensing observations. Several ML-based studies have demonstrated improved performance over traditional IME methods by directly learning the relationship between methane enhancement maps and emission rates (Jongaramrungruang et al., 2022; Radman et al., 2023; Joyce et al., 2023). These approaches typically utilize convolutional neural networks (CNNs), often in U-Net or ResNet-based architectures, to extract spatial features from hyperspectral and multispectral images. Some models further incorporate auxiliary information, such as wind speed, land surface reflectance, and plume morphology, to refine predictions. However, despite these advancements, ML-based methods also exhibit systematic biases, particularly in the underestimation of high-emission sources (Bruno et al., 2023; Si et al., 2024). This underestimation is attributed to the inherent smoothing effect of neural networks, which tend to reduce variance in predictions and struggle with extreme values.

A critical challenge in comparing different ML-based flux estimation methods is the lack of standardized datasets and evaluation metrics. Unlike plume segmentation tasks, where benchmark datasets such as AVIRIS-NG and Sentinel-2 annotated plumes are available, emission rate

estimation datasets are often derived from simulated methane plumes superimposed onto real satellite images (Radman et al., 2023; Si et al., 2024). These synthetic datasets are essential for training ML models but may not fully capture the complexities of real-world plume dynamics, leading to discrepancies when models are applied to actual observations. Furthermore, different studies employ various evaluation metrics, including mean absolute percentage error (MAPE), root mean square error (RMSE), and correlation coefficients, making direct performance comparisons difficult. Some studies report performance graphically rather than providing numerical benchmarks, further complicating reproducibility and assessment.

Another open question in ML-based flux estimation is whether incorporating wind data into model training improves or degrades overall accuracy. Traditional methods explicitly require wind information, but several ML models have demonstrated robust performance without it (Jongaramrungruang et al., 2022; Bruno et al., 2023). In contrast, some studies find that including wind speed as an additional input feature can enhance model predictions, especially for low-emission sources where dispersion effects dominate (Joyce et al., 2023). However, the uncertainty associated with wind speed estimation remains a critical factor. For instance, Bruno et al. (2023) found that the wind direction had minimal impact on ML-based flux estimation, whereas wind speed errors dominated at velocities below 4 m/s. This suggests that while ML models may be less sensitive to wind-related errors than IME, their effectiveness still depends on the quality and reliability of ancillary meteorological data.

To advance the field of ML-based methane flux estimation, future research should focus on developing standardised, open-access reference datasets that encompass a diverse range of emission sources, atmospheric conditions, and sensor types. Additionally, hybrid approaches that integrate physics-based priors with data-driven ML models could improve generalisation and reduce systematic biases. For example, combining ML-based segmentation with traditional flux inversion techniques could leverage the strengths of both methodologies, enhancing reliability across different remote sensing platforms. More studies are also needed to quantify the impact of spatial resolution, spectral information, and wind uncertainty on ML model performance. By addressing these challenges, ML techniques may have the potential to improve methane emission estimates, but more research is needed to fully assess its capabilities.

2.6 Application of uncertainty estimates

The inclusion of uncertainty information associated to flux rate estimates has not just informative purposes but it has direct impact on multiple application areas such as flux area inversions or conformance testing. A non-exhaustive list of potential applications of flux rate uncertainty includes:

- *Use of plume imager data in inversions of flux mappers data* which is dependent on the information of the error covariance (both for prior and observation data). For example,

recent work in (Naus et al., 2023) has not only considered inventory data for the prior but complemented that information with S2 plume information. Efforts in a better estimation of flux rate uncertainty and spatial error correlation could improve the a-posteriori flux maps and associated error covariance.

- *Integrated emissions monitoring* The monitoring of emissions using multiple missions such as the recent works in Cusworth et al. (2021) or Guanter et al. (2024) will be expanded with the advent of operational hyperspectral missions such as CHIME. In this scenario, the detailed uncertainty assessment and error correlation will be key to report an integrated methane emission over a time period or the entire release. Reliable uncertainty estimates would not only be useful to set the emission in context but will also determine the extent of applicability of upcoming emissions regulations.
- *Validation and inter-comparison of flux rate estimates*. The sole comparison of two measurements does not provide sufficient information to determine the agreement between measurements. The consideration of uncertainty in both the reference and target measurement triggers the possibility to include a more quantitative assessment of the comparison such as those proposed in a conformance test JCGM (2012).

3 WP2 initial uncertainty estimates methodology

3.1 UPV

The flux rate uncertainty estimates are calculated from the individual contributions of IME and U_{eff}. These contributions are combined with either the law of propagation of uncertainty (LPU) or Monte Carlo propagation treating the different contributions as uncorrelated. Both the accuracy of the IME model itself and the length scale L of the plume are not considered. The same methodology is applied for both plume imagers and flux mappers.

The standard uncertainty of the IME is estimated from the standard deviation of $\Delta XCH4$ across plume-free regions of the imaged area. Alternatively, a large region-of-interest can be considered if the plume and possible outliers can be considered of negligible impact (i.e. sparsity can be assumed).

The U_{eff} uncertainty is obtained from the propagation of U_{10} uncertainty through the calibration coefficients. An uncertainty *k*=1 of 0.05 is assigned to the calibration coefficients as in Sánchez-García et al. (2022). This is a proxy of the regression sensitivity to different atmospheric parameterisation, flux rate ranges or noise levels as discussed in Gorroño et al. (2023).

For U_{10}, an uncertainty of 2 m/s has been assigned based on the values reported in Varon et al. (2018). This study compared local wind speed values measured at different airports with the GEOS-FP values. More recently, the study in Guanter et al. (2024) set a U_{10} uncertainty value

of 2 m/s for values equal or higher than 4 m/s based on the validation of MERRA-2 products in Carvalho (2019). For values below 4 m/s a relative uncertainty of 50% (k=1) is assigned and the error distribution is capped at positive values to consider physically possible values.

The estimation of the uncertainty associated with the total emission is the result of propagating the uncertainty using a multivariate Monte Carlo methodology. That is several samples from each flux rate estimate are generated considering error correlation among them. Then, they are propagated through the flux rate interpolation/fitting and curve integration to determine the error distribution at the output. We assume a 50% correlation between flux rate errors in order to account for both uncorrelated error components (e.g. plume shape changes) and correlated error components (e.g. same source area). No uncertainty has been allocated to the interpolation/fitting process itself.

3.2 SRON

3.2.1 SRON algorithm uncertainty for PRISMA, EnMAP, and EMIT

There are three sources of uncertainty in our emission uncertainty estimations: wind speed uncertainty, random uncertainty of the retrieval, and uncertainty in the IME calibration (Varon et al., 2019, 2020; Maasakkers et al., 2022).

To parameterize the uncertainty in the wind speed, we compare the European Centre for Medium-Range Weather Forecasts Reanalysis 5 (ERA5) 10-m wind data with the automated Surface Observing System (ASOS) dataset obtained from worldwide airports. We only include the wind data recorded between 10:00 and 14:00 (local time) to coincide with overpass times of hyperspectral instruments. The standard deviation of the difference between ERA5 and ASOS wind data is $\sim$1.5 m/s for wind speeds higher than 3 m/s. For wind speeds lower than 3 m/s, we apply a relative wind uncertainty of 50% (Varon et al., 2018). We also compare the ERA5 and GEOS Forward Processing (GEOS-FP) wind reanalysis data and find that their difference falls within our wind uncertainty estimate.

To quantify the effects of random retrieval error, we apply the plume mask to non-plume pixels across the entire scene and calculate the standard deviation of the resulting emission rates (Varon et al., 2019).

The last component of the uncertainty is the IME calibration error. The area-source calibration that we use for landfills assumes a uniform distribution of methane emissions across a 275$\times$275 m^2 area, whereas the realistic distribution can be more complex (Maasakkers et al., 2022). To estimate the uncertainty originating from this simplification, we change the effective wind calibration we use to one that was calibrated using point sources and calculate the resulting change in emission rate. For the point-source calibration, we use the average fit residuals to calculate the emission rate uncertainties for each satellite instrument.

To estimate the uncertainty in individual emission rate estimates, we calculate the square root of the sum of the squares of the individual uncertainties.

3.2.2 SRON algorithm uncertainty for TROPOMI/S-5P

For our operationally detected plumes, emissions are automatically quantified using the Integrated Mass Enhancement (IME, Varon et al. (2018)) method. It relates the plume emission rate Q with the excess of methane contained in the plume mask denoted as IME, with the plume length L defined as the square-root of the mask area and with the effective wind speed U_{eff}, calibrated on atmospheric transport simulations against the 10-m wind speed U_{10} or the wind speed averaged over the Planetary Boundary Layer U_{PBL}. We have Eq. 2.2; with:

$$U_{\text{eff}} = 0.47 \cdot U_{\text{PBL}} + 0.31 \text{ or } U_{\text{eff}} = 0.59 \cdot U_{10} \tag{3.1}$$

The IME method is used in an ensemble approach, yielding an average emission rate and an uncertainty estimate (Schuit et al., 2023). We vary the following IME method inputs to build the ensemble:

- The wind speed product:
  - ERA5 10m wind speed (Hersbach et al., 2020)
  - GEOS-FP 10m wind speed (Molod et al., 2012)
  - GEOS-FP PBL wind speed (Molod et al., 2012).
- The plume masking approach employed by SRON is fully automated. Given a scene with a positive detection, the Class Activation Map provided by our machine learning detection method is multiplied by the methane enhancement map. The pixel corresponding to the maximum of this multiplication is the seed of the plume mask. We then employ an iterative outward dilation approach starting from this seed to include all pixels for which the methane enhancement is above a certain threshold.

  We consider the plume masking as part of our uncertainty ensemble by varying the enhancement threshold for a pixel to be included in the plume mask, ranging from 1.3 to 2.4 standard deviations of the background concentration, in 0.1 steps.
- The background concentration used to yield enhancement values, by ± 2 times the mean uncertainty of the scene, in 0.4 steps.
- The wind speed values, from -50% to +50%, in 10% steps.
- The effective wind speed calibration coefficients, from -5% to 5%, in 1% steps.

This yields an ensemble with 43.923 members, from which the average is used for the reported emission rate and the standard deviation as uncertainty estimate.

3.3 Kayrros

3.3.1 Kayrros algorithm uncertainty for high-resolution imagers

Methane plume detections by high-resolution imagers are quantified using the IME method combined with the European Centre for Medium-Range Weather Forecasts Reanalysis 5 (ERA5) 10-m wind data (Hersbach et al., 2020). The flux rate uncertainty estimates are calculated from the individual contributions of IME and the wind data. Since plume delineations are made by a deep learning model, whose detections may eventually be corrected by a human expert analyst, the uncertainty on the parameter L is not estimated at the moment. This would require to isolate the uncertainties coming from the deep learning model and the biased uncertainty depending on the individual human expert validating the plume mask.

On one hand, the retrieval noise in $\Delta XCH4$ is assumed to be homogeneous and independent across pixels and to follow a normal distribution of parameter σ. This parameter is estimated as the empirical standard deviation $\tilde{\sigma}$ of methane-free pixels in $\Delta XCH4$. The independence of noise across pixels allows to eventually combine this estimate on the N pixels of the detected plume $\sigma_{IME} = k\sqrt{N}\tilde{\sigma}$.

On the other hand, the wind uncertainty is estimated by assuming an individual empirical uncertainty of 0.5 m/s on each component of the ERA5 10-m wind data. This uncertainty is then propagated in the effective wind speed computation using the appropriate formula for each sensor.

Eventually, the uncertainties are combined in quadrature to give the final flux rate uncertainty

$$\frac{\sigma_{flow}}{flow} = \sqrt{\left(\frac{\sigma_{U_{eff}}}{U_{eff}}\right)^2 + \left(\frac{\sigma_{IME}}{IME}\right)^2}$$

3.3.2 Kayrros algorithm uncertainty for TROPOMI/S-5P

Flux rate estimation of Sentinel-5P plumes are done by computing the methane enhancements by estimating the background, and then simulating this enhancement using the Lagrangian particle dispersion model HYSPLIT. The model simulates plumes originating from the labeled source location, and the meteorological data used for the HYSPLIT simulations come from the Global Forecast System (GFS) by the National Centers for Environmental Prediction (NCEP) at 0.25-degree and hourly resolutions. Further details on the quantification methodology can be found in Lauvaux et al. (2022).

Uncertainty in flux rate estimation mainly stems from uncertainty in the model input parameters, namely:

- uncertainty $\sigma_{measure}$ on the Sentinel-5P measurements

- uncertainty $\sigma_{weather}$ in meteorological data driving the HYSPLIT simulations
- uncertainty σ_{offset} in the duration of the simulation reflecting the duration of the emission
- uncertainty $\sigma_{background}$ in background quantification
- uncertainty $\sigma_{location}$ in longitude and latitude source location estimation

In order to evaluate the magnitude of these variations, a sensitivity analysis has been run on a random set of methane plumes. For each parameter bringing uncertainty to the flux rate estimate, an ensemble of simulation has been built with different values for the concerned parameter. The uncertainty associated with the parameter is taken as the standard deviation of the ensemble. Assuming each of these uncertainty sources is independent, the total uncertainty is obtained by propagating the individual uncertainty estimates.

$$\sigma_{total} = \sqrt{\sigma^2_{measure} + \sigma^2_{weather} + \sigma^2_{offset} + \sigma^2_{background} + \sigma^2_{location}}$$

3.4 GHGSat

The uncertainty σ_Q on the retrieved emission rate $\hat{Q}$ is estimated by a quadrature sum of 3 individual error contributions:

$$\sigma_{\mathrm{tot}} = \sqrt{\sigma^2_{\mathrm{meas}} + \sigma^2_{\mathrm{wind}} + \sigma^2_{\mathrm{mod}}}, \tag{3.2}$$

where σ_{meas} is the measurement error associated with imperfect knowledge of methane column density in the level 2 retrieval, σ_{wind} is the error caused by wind speed uncertainty, and σ_{mod} is the modeling error associated with the IME to source rate conversion.

The measurement error is driven by the presence of noise in the retrieved column density field, including shot noise, camera read noise, and other ground-correlated noise sources. To quantify its effect on rate retrieval for a particular plume observation, we must account for the aggregation of the column errors within the plume mask (IME calculation). We do this by moving the plume mask to an ensemble of nonplume locations across the imaging domain, from which we infer the error distribution for our source rate estimate Varon et al. (2019). More specifically, for each plume, we define a grid of rectangular tiles that have the same size as the plume bounding box, and cover the full domain of the retrieval. For each tile, we apply equation (2.2) and compute a dummy source rate for each. Ground cells that are quality-flagged or part of the true plume mask are excluded from the calculation. We then compute the mean $\bar{Q}_{\mathrm{tiles}}$ variance $\sigma^2_{\mathrm{tiles}}$ on all tiles to provide an estimate of bias and uncertainty. The mean rate is used to correct for global biases by subtracting it from the initial estimation. The measurement error can be expressed as

$$\sigma_{\mathrm{meas}} = \sqrt{\sigma^2_{\mathrm{tiles}} + \frac{\sigma^2_{\mathrm{tiles}}}{N_{\mathrm{tiles}}}}, \tag{3.3}$$

where the second term in the radical reflects the error on the bias correction when N_{tiles} dummy source rates have been used for bias and uncertainty estimations.

Wind speed error arises from using a coarse resolution meteorological database to estimate the local 10-m wind speed U_{10}. This error propagates through the effective wind speed function $U_{\text{eff}} = f(U_{10})$ to affect the retrieved source rate. Wind speed error tends to dominate the overall uncertainty in retrieved source rates. It was evaluated following the approach by Varon et al. (2018), by comparing the values queried from the wind database with high-fidelity wind speed measurements from weather stations. The wind uncertainty was found to be wind-speed dependent, which is modeled using a second order polynomial over the 0 to 12.5 m/s range with linear extrapolation to higher wind speeds.

Model error stems from the imperfection of the mapping from U_{10} to U_{eff} , for plumes of varying shapes and sizes in different meteorological conditions. An error analysis was conducted by Varon et al. (2018, 2019) using a large ensemble of simulated plumes in various atmospheric conditions. The average relative error was found to be around 7% for the IME method, which is the value used for σ_{mod} across observations.

3.5 IUP-UB

3.5.1 IUP-UB algorithm uncertainty for PRISMA and EnMAP

Atmospheric methane anomalies are retrieved using a retrieval algorithm which is still under development. At present several methods are under investigation and this set of algorithms is currently referred to as HiFi ("HighResolutionFit"). HiFi is based on fitting parameters of a forward model ("F") to the measured radiance spectra considering the measurement error covariance matrix ("S_ϵ"). One of these methods is the Matched Filter (MF) method (see Roger et al. (2024b)) referred to as HiFi/MF.

Emissions are derived from the retrieved atmospheric methane anomalies using a Cross-Sectional-Flux (CSF) algorithm similar as described in Schneising et al. (2020, 2024) and Fuentes Andrade et al. (2024).

The CSF method emission uncertainty considers three contributions and the corresponding uncertainty components are added root-sum-square assuming they are uncorrelated. These uncertainty components are:

- Wind uncertainty: Considers temporal wind variability within a few hours before and after the satellite observation plus a constant value (0.5 m/s) for overall wind uncertainty.
- Dispersion: Considers turbulence and other effects leading to variability of the fluxes as obtained from the individual CSF cross-sections (see Fuentes Andrade et al. (2024)).
- Other error terms including algorithm sensitivity: Here we use a constant relative uncer-

tainty of 20% based on numerical experience by changing parameters or setting controlling the algorithm. For emissions from single satellite overpasses, we consider this the minimum relative error that can be realistically achieved and this error term also considers this.

3.5.2 IUP-UB algorithm uncertainty for TROPOMI/S-5P

We use for TROPOMI XCH4 the WFMD v1.8 data product described in Schneising et al. (2023).

Emissions are derived from the retrieved XCH4 using a Cross-Sectional-Flux (CSF) algorithm similar as described in Schneising et al. (2020, 2024) and Fuentes Andrade et al. (2024).

The CSF method emission uncertainty considers three contributions and the corresponding uncertainty components are added root-sum-square assuming they are uncorrelated. These uncertainty components are:

- Wind uncertainty: Considers temporal wind variability within a few hours before and after the satellite observation plus a constant value (0.5 m/s) for overall wind uncertainty.
- Dispersion: Considers turbulence and other effects leading to variability of the fluxes as obtained from the individual CSF cross-sections (see Fuentes Andrade et al. (2024)).
- Other error terms including algorithm sensitivity: Here we use a constant relative uncertainty of 20% based on numerical experience by changing parameters or setting controlling the algorithm. For emissions from single satellite overpasses, we consider this the minimum relative error than can be realistically achieved and this error term also considers this.

4 Summary

This document briefly summarises the state-of-the-art uncertainty estimates associated with the flux rate of point-source methane emissions. The literature is scarce since, at the time of writing, the detection and quantification of this type of emissions is very recent, with many methodologies under development. Section 2 reviews the current literature on methane flux uncertainty. Although not a large number of dedicated studies were found, it is possible to find relevant information on specific uncertainty contributions. These contributions mainly refer to the retrieval noise, the U_{eff} uncertainty, and the U_{10} uncertainty. These can be defined in sensitivity analysis, measuring directly over the scene (e.g., retrieval noise), and sometimes are vaguely defined with either a rough estimate or an expert guess. Little or no information could be found related to the error correlation within these uncertainty contributions and the spatiotemporal error correlation of

methane flux rates. The subsection 2.6, briefly defines the potential uses of these uncertainties. These not only better inform the users, but can also better constrain inversions of flux mappers data, support the spatiotemporal integration of emissions, and the validation of methane flux rates.

The different participants in the MEDUSA project have described their current uncertainty methodology in Section 3. These are the uncertainty estimates that will be used in the validation and intercomparison for WP2 within this project. This document is our starting point for defining a robust uncertainty methodology that can provide more credibility to estimated methane emissions. They will be directly used to improve the uncertainty and better define the validation and inter-comparison in WP2.

5 References

Ayasse, A., Cusworth, D., Howell, K., O'Neill, K., Conrad, B., Johnson, M., Asner, G., Duren, R., 07 2024. Probability of detection and multi-sensor persistence of methane emissions from coincident airborne and satellite observations. EarthArxiv.

Balasus, N., Jacob, D. J., Lorente, A., Maasakkers, J. D., Parker, R. J., Boesch, H., Chen, Z., Kelp, M. M., Nesser, H., Varon, D. J., 2023. A blended tropomi+gosat satellite data product for atmospheric methane using machine learning to correct retrieval biases. Atmospheric Measurement Techniques 16 (16), 3787–3807.
URL https://amt.copernicus.org/articles/16/3787/2023/

BIPM, I., IFCC, I., ISO, I., IUPAP, O., 2011. Evaluation of measurement data—supplement 2 to the 'guide to the expression of uncertainty in measurement'—extension to any number of output quantities. JCGM 102, 2011.

Borchardt, J., Gerilowski, K., Krautwurst, S., Bovensmann, H., Thorpe, A. K., Thompson, D. R., Frankenberg, C., Miller, C. E., Duren, R. M., Burrows, J. P., 2021. Detection and quantification of ch_4 plumes using the wfm-doas retrieval on aviris-ng hyperspectral data. Atmospheric Measurement Techniques 14 (2), 1267–1291.
URL https://amt.copernicus.org/articles/14/1267/2021/

Bruno, J., Jervis, D., Varon, D., Jacob, D., 2023. U-plume: Automated algorithm for plume detection and source quantification by satellite point-source imagers. EGUsphere 2023, 1–24.

Carvalho, D., 2019. An assessment of nasa's gmao merra-2 reanalysis surface winds. Journal of Climate 32 (23), 8261 – 8281.
URL https://journals.ametsoc.org/view/journals/clim/32/23/jcli-d-19-0199.1.xml

Conrad, B. M., Tyner, D. R., Johnson, M. R., 2023. Robust probabilities of detection and quantification uncertainty for aerial methane detection: Examples for three airborne technologies. Remote Sensing of Environment 288, 113499.
URL https://www.sciencedirect.com/science/article/pii/S0034425723000500

Cusworth, D. H., Duren, R. M., Thorpe, A. K., Pandey, S., Maasakkers, J. D., Aben, I., Jervis, D., Varon, D. J., Jacob, D. J., Randles, C. A., Gautam, R., Omara, M., Schade, G. W., Dennison, P. E., Frankenberg, C., Gordon, D., Lopinto, E., Miller, C. E., 2021. Multisatellite imaging of a gas well blowout enables quantification of total methane emissions. Geophysical Research Letters 48 (2), e2020GL090864, e2020GL090864 2020GL090864.
URL https://agupubs.onlinelibrary.wiley.com/doi/abs/10.1029/2020GL090864

Cusworth, D. H., Jacob, D. J., Varon, D. J., Chan Miller, C., Liu, X., Chance, K., Thorpe, A. K., Duren, R. M., Miller, C. E., Thompson, D. R., Frankenberg, C., Guanter, L., Randles, C. A., 2019. Potential of next-generation imaging spectrometers to detect and quantify methane point sources from space. Atmospheric Measurement Techniques 12 (10), 5655–5668.
URL https://amt.copernicus.org/articles/12/5655/2019/

Davis, N. N., Badger, J., Hahmann, A. N., Hansen, B. O., Mortensen, N. G., Kelly, M., Larsén, X. G., Olsen, B. T., Floors, R., Lizcano, G., Casso, P., Lacave, O., Bosch, A., Bauwens, I., Knight, O. J., van Loon, A. P., Fox, R., Parvanyan, T., Hansen, S. B. K., Heathfield, D., Onninen, M., Drummond, R., 2023. The global wind atlas: A high-resolution dataset of climatologies and associated web-based application. Bulletin of the American Meteorological Society 104 (8), E1507 – E1525.
URL https://journals.ametsoc.org/view/journals/bams/104/8/BAMS-D-21-0075.1.xml

Fahlen, J. E., Brodrick, P. G., Coleman, R. W., Elder, C. D., Thompson, D. R., Thorpe, A. K., Green, R. O., Green, J. J., Lopez, A. M., Xiang, C., 2024. Sensitivity and uncertainty in matched-filter-based gas detection with imaging spectroscopy. IEEE Transactions on Geoscience and Remote Sensing 62, 1–10.

Foote, M. D., Dennison, P. E., Thorpe, A. K., Thompson, D. R., Jongaramrungruang, S., Frankenberg, C., Joshi, S. C., 2020. Fast and accurate retrieval of methane concentration from imaging spectrometer data using sparsity prior. IEEE Transactions on Geoscience and Remote Sensing 58 (9), 6480–6492.

Frankenberg, C., Platt, U., Wagner, T., 2005. Iterative maximum a posteriori (imap)-doas for retrieval of strongly absorbing trace gases: Model studies for ch_4 and co_2 retrieval from near infrared spectra of sciamachy onboard envisat. Atmospheric Chemistry and Physics 5 (1), 9–22.
URL https://acp.copernicus.org/articles/5/9/2005/

Frankenberg, C., Thorpe, A. K., Thompson, D. R., Hulley, G., Kort, E. A., Vance, N., Borchardt, J., Krings, T., Gerilowski, K., Sweeney, C., Conley, S., Bue, B. D., Aubrey, A. D., Hook, S., Green, R. O., 2016. Airborne methane remote measurements reveal heavy-tail flux distribution in four corners region. Proceedings of the National Academy of Sciences 113 (35), 9734–9739.
URL https://www.pnas.org/content/113/35/9734

Fuentes Andrade, B., Buchwitz, M., Reuter, M., Bovensmann, H., Richter, A., Boesch, H., Burrows, J. P., 2024. A method for estimating localized co_2 emissions from co-located satellite xco_2 and no_2 images. Atmospheric Measurement Techniques 17 (3), 1145–1173.
URL https://amt.copernicus.org/articles/17/1145/2024/

Gorroño, J., Varon, D. J., Irakulis-Loitxate, I., Guanter, L., 2023. Understanding the potential of Sentinel-2 for monitoring methane point emissions. Atmospheric Measurement Techniques

16 (1), 89–107.
URL https://amt.copernicus.org/articles/16/89/2023/

Guanter, L., Irakulis-Loitxate, I., Gorroño, J., Sánchez-García, E., Cusworth, D. H., Varon, D. J., Cogliati, S., Colombo, R., 2021. Mapping methane point emissions with the prisma spaceborne imaging spectrometer. Remote Sensing of Environment 265, 112671.
URL https://www.sciencedirect.com/science/article/pii/S0034425721003916

Guanter, L., Roger, J., Sharma, S., Valverde, A., Irakulis-Loitxate, I., Gorroño, J., Zhang, X., Schuit, B. J., Maasakkers, J. D., Aben, I., Groshenry, A., Benoit, A., Peyle, Q., Zavala-Araiza, D., 2024. Multisatellite data depicts a record-breaking methane leak from a well blowout. Environmental Science & Technology Letters 11 (8), 825–830.
URL https://doi.org/10.1021/acs.estlett.4c00399

Hald, C., Zeeman, M., Laux, P., Mauder, M., Kunstmann, H., 2019. Large-eddy simulations of real-world episodes in complex terrain based on era-reanalysis and validated by ground-based remote sensing data. Monthly Weather Review 147 (12), 4325 – 4343.
URL https://journals.ametsoc.org/view/journals/mwre/147/12/mwr-d-19-0016.1.xml

Hersbach, H., Bell, B., Berrisford, P., Hirahara, S., Horányi, A., Muñoz-Sabater, J., Nicolas, J., Peubey, C., Radu, R., Schepers, D., Simmons, A., Soci, C., Abdalla, S., Abellan, X., Balsamo, G., Bechtold, P., Biavati, G., Bidlot, J., Bonavita, M., De Chiara, G., Dahlgren, P., Dee, D., Diamantakis, M., Dragani, R., Flemming, J., Forbes, R., Fuentes, M., Geer, A., Haimberger, L., Healy, S., Hogan, R. J., Hólm, E., Janisková, M., Keeley, S., Laloyaux, P., Lopez, P., Lupu, C., Radnoti, G., de Rosnay, P., Rozum, I., Vamborg, F., Villaume, S., Thépaut, J.-N., 2020. The era5 global reanalysis. Quarterly Journal of the Royal Meteorological Society 146 (730), 1999–2049.
URL https://rmets.onlinelibrary.wiley.com/doi/abs/10.1002/qj.3803

Hu, H., Hasekamp, O., Butz, A., Galli, A., Landgraf, J., Aan de Brugh, J., Borsdorff, T., Scheepmaker, R., Aben, I., 2016. The operational methane retrieval algorithm for tropomi. Atmospheric Measurement Techniques 9 (11), 5423–5440.
URL https://amt.copernicus.org/articles/9/5423/2016/

Irakulis-Loitxate, I., Guanter, L., Liu, Y.-N., Varon, D. J., Maasakkers, J. D., Zhang, Y., Chulakadabba, A., Wofsy, S. C., Thorpe, A. K., Duren, R. M., Frankenberg, C., Lyon, D. R., Hmiel, B., Cusworth, D. H., Zhang, Y., Segl, K., Gorroño, J., Sánchez-García, E., Sulprizio, M. P., Cao, K., Zhu, H., Liang, J., Li, X., Aben, I., Jacob, D. J., 2021. Satellite-based survey of extreme methane emissions in the permian basin. Science Advances 7 (27).
URL https://advances.sciencemag.org/content/7/27/eabf4507

JCGM, 2008. Evaluation of measurement data — Supplement 1 to the “Guide to the expression of uncertainty in measurement” — Propagation of distributions using a Monte Carlo method. Tech. Rep. 101.

JCGM, 2012. Evaluation of measurement data - The role of measurement uncertainty in conformity assessment. Tech. Rep. 106.
URL https://www.bipm.org/en/doi/10.59161/jcgm106-2012

Jervis, D., McKeever, J., Durak, B. O. A., Sloan, J. J., Gains, D., Varon, D. J., Ramier, A., Strupler, M., Tarrant, E., 2021. The ghgsat-d imaging spectrometer. Atmospheric Measurement Techniques 14 (3), 2127–2140.
URL https://amt.copernicus.org/articles/14/2127/2021/

Jongaramrungruang, S., Matheou, G., Thorpe, A. K., Zeng, Z.-C., Frankenberg, C., 2021. Remote sensing of methane plumes: instrument tradeoff analysis for detecting and quantifying local sources at global scale. Atmospheric Measurement Techniques 14 (12), 7999–8017.
URL https://amt.copernicus.org/articles/14/7999/2021/

Jongaramrungruang, S., Thorpe, A. K., Matheou, G., Frankenberg, C., 2022. Methanet – an ai-driven approach to quantifying methane point-source emission from high-resolution 2-d plume imagery. Remote Sensing of Environment 269, 112809.
URL https://www.sciencedirect.com/science/article/pii/S0034425721005290

Joyce, P., Ruiz Villena, C., Huang, Y., Webb, A., Gloor, M., Wagner, F. H., Chipperfield, M. P., Barrio Guilló, R., Wilson, C., Boesch, H., 2023. Using a deep neural network to detect methane point sources and quantify emissions from prisma hyperspectral satellite images. Atmospheric Measurement Techniques 16 (10), 2627–2640.
URL https://amt.copernicus.org/articles/16/2627/2023/

Krings, T., Gerilowski, K., Buchwitz, M., Reuter, M., Tretner, A., Erzinger, J., Heinze, D., Pflüger, U., Burrows, J. P., Bovensmann, H., 2011. Mamap – a new spectrometer system for column-averaged methane and carbon dioxide observations from aircraft: retrieval algorithm and first inversions for point source emission rates. Atmospheric Measurement Techniques 4 (9), 1735–1758.
URL https://amt.copernicus.org/articles/4/1735/2011/

Lauvaux, T., Giron, C., Mazzolini, M., d'Aspremont, A., Duren, R., Cusworth, D., Shindell, D., Ciais, P., 2022. Global assessment of oil and gas methane ultra-emitters. Science 375 (6580), 557–561.
URL https://www.science.org/doi/abs/10.1126/science.abj4351

Lorente, A., Borsdorff, T., Martinez-Velarte, M. C., Landgraf, J., 2023. Accounting for surface reflectance spectral features in tropomi methane retrievals. Atmospheric Measurement Techniques 16 (6), 1597–1608.
URL https://amt.copernicus.org/articles/16/1597/2023/

Maasakkers, J. D., McDuffie, E. E., Sulprizio, M. P., Chen, C., Schultz, M., Brunelle, L., Thrush, R., Steller, J., Sherry, C., Jacob, D. J., Jeong, S., Irving, B., Weitz, M., 2023. A gridded inven-

tory of annual 2012–2018 u.s. anthropogenic methane emissions. Environmental Science & Technology 57 (43), 16276–16288, pMID: 37857355.
URL https://doi.org/10.1021/acs.est.3c05138

Maasakkers, J. D., Varon, D. J., Elfarsdóttir, A., McKeever, J., Jervis, D., Mahapatra, G., Pandey, S., Lorente, A., Borsdorff, T., Foorthuis, L. R., Schuit, B. J., Tol, P., van Kempen, T. A., van Hees, R., Aben, I., 2022. Using satellites to uncover large methane emissions from landfills. Science Advances 8 (32), eabn9683.
URL https://www.science.org/doi/abs/10.1126/sciadv.abn9683

MacLeod, D. A., Cloke, H. L., Pappenberger, F., Weisheimer, A., 2016. Improved seasonal prediction of the hot summer of 2003 over europe through better representation of uncertainty in the land surface. Quarterly Journal of the Royal Meteorological Society 142 (694), 79–90.
URL https://rmets.onlinelibrary.wiley.com/doi/abs/10.1002/qj.2631

Markham, B. L., 1985. The landsat sensors' spatial responses. IEEE Transactions on Geoscience and Remote Sensing GE-23 (6), 864–875.

Molod, A., Takacs, L., Suarez, M., Bacmeister, J., Song, I.-S., Eichmann, A., 2012. The geos-5 atmospheric general circulation model: Mean climate and development from merra to fortuna. Tech. rep.

Muñoz Sabater, J., Dutra, E., Agustí-Panareda, A., Albergel, C., Arduini, G., Balsamo, G., Boussetta, S., Choulga, M., Harrigan, S., Hersbach, H., Martens, B., Miralles, D. G., Piles, M., Rodríguez-Fernández, N. J., Zsoter, E., Buontempo, C., Thépaut, J.-N., 2021. Era5-land: a state-of-the-art global reanalysis dataset for land applications. Earth System Science Data 13 (9), 4349–4383.
URL https://essd.copernicus.org/articles/13/4349/2021/

Naus, S., Maasakkers, J. D., Gautam, R., Omara, M., Stikker, R., Veenstra, A. K., Nathan, B., Irakulis-Loitxate, I., Guanter, L., Pandey, S., Girard, M., Lorente, A., Borsdorff, T., Aben, I., 2023. Assessing the relative importance of satellite-detected methane superemitters in quantifying total emissions for oil and gas production areas in algeria. Environmental Science & Technology 57 (48), 19545–19556, pMID: 37956986.
URL https://doi.org/10.1021/acs.est.3c04746

Pandey, S., Gautam, R., Houweling, S., van der Gon, H. D., Sadavarte, P., Borsdorff, T., Hasekamp, O., Landgraf, J., Tol, P., van Kempen, T., Hoogeveen, R., van Hees, R., Hamburg, S. P., Maasakkers, J. D., Aben, I., 2019. Satellite observations reveal extreme methane leakage from a natural gas well blowout. Proceedings of the National Academy of Sciences 116 (52), 26376–26381.
URL https://www.pnas.org/content/116/52/26376

Radman, A., Mahdianpari, M., Varon, D. J., Mohammadimanesh, F., 2023. S2metnet: A novel dataset and deep learning benchmark for methane point source quantification using sentinel-2 satellite imagery. Remote Sensing of Environment 295, 113708.

Roger, J., Guanter, L., Gorroño, J., Irakulis-Loitxate, I., 2024a. Exploiting the entire near-infrared spectral range to improve the detection of methane plumes with high-resolution imaging spectrometers. Atmospheric Measurement Techniques 17 (4), 1333–1346.
URL https://amt.copernicus.org/articles/17/1333/2024/

Roger, J., Irakulis-Loitxate, I., Valverde, A., Gorroño, J., Chabrillat, S., Brell, M., Guanter, L., 2024b. High-resolution methane mapping with the enmap satellite imaging spectroscopy mission. IEEE Transactions on Geoscience and Remote Sensing 62, 1–12.

Sánchez-García, E., Gorroño, J., Irakulis-Loitxate, I., Varon, D. J., Guanter, L., 2022. Mapping methane plumes at very high spatial resolution with the worldview-3 satellite. Atmospheric Measurement Techniques 15 (6), 1657–1674.
URL https://amt.copernicus.org/articles/15/1657/2022/

Schneising, O., Buchwitz, M., Hachmeister, J., Vanselow, S., Reuter, M., Buschmann, M., Bovensmann, H., Burrows, J. P., 2023. Advances in retrieving xch$_4$ and xco from sentinel-5 precursor: improvements in the scientific tropomi/wfmd algorithm. Atmospheric Measurement Techniques 16 (3), 669–694.
URL https://amt.copernicus.org/articles/16/669/2023/

Schneising, O., Buchwitz, M., Reuter, M., Bovensmann, H., Burrows, J. P., Borsdorff, T., Deutscher, N. M., Feist, D. G., Griffith, D. W. T., Hase, F., Hermans, C., Iraci, L. T., Kivi, R., Landgraf, J., Morino, I., Notholt, J., Petri, C., Pollard, D. F., Roche, S., Shiomi, K., Strong, K., Sussmann, R., Velazco, V. A., Warneke, T., Wunch, D., 2019. A scientific algorithm to simultaneously retrieve carbon monoxide and methane from tropomi onboard sentinel-5 precursor. Atmospheric Measurement Techniques 12 (12), 6771–6802.
URL https://amt.copernicus.org/articles/12/6771/2019/

Schneising, O., Buchwitz, M., Reuter, M., Vanselow, S., Bovensmann, H., Burrows, J. P., 2020. Remote sensing of methane leakage from natural gas and petroleum systems revisited. Atmospheric Chemistry and Physics 20 (15), 9169–9182.
URL https://acp.copernicus.org/articles/20/9169/2020/

Schneising, O., Buchwitz, M., Reuter, M., Weimer, M., Bovensmann, H., Burrows, J. P., Bösch, H., 2024. Towards a sector-specific co/co$_2$ emission ratio: satellite-based observations of co release from steel production in germany. Atmospheric Chemistry and Physics 24 (13), 7609–7621.
URL https://acp.copernicus.org/articles/24/7609/2024/

Schuit, B. J., Maasakkers, J. D., Bijl, P., Mahapatra, G., van den Berg, A.-W., Pandey, S., Lorente, A., Borsdorff, T., Houweling, S., Varon, D. J., McKeever, J., Jervis, D., Girard, M., Irakulis-Loitxate, I., Gorroño, J., Guanter, L., Cusworth, D. H., Aben, I., 2023. Automated detection and monitoring of methane super-emitters using satellite data. Atmospheric Chemistry and Physics 23 (16), 9071–9098.
URL https://acp.copernicus.org/articles/23/9071/2023/

Schwaerzel, M., Emde, C., Brunner, D., Morales, R., Wagner, T., Berne, A., Buchmann, B., Kuhlmann, G., 2020. Three-dimensional radiative transfer effects on airborne and ground-based trace gas remote sensing. Atmospheric Measurement Techniques 13 (8), 4277–4293.
URL https://amt.copernicus.org/articles/13/4277/2020/

Si, G., Fu, S., Yao, W., 2024. Unlocking the potential: Multi-task deep learning for spaceborne quantitative monitoring of fugitive methane plumes. arXiv preprint arXiv:2401.12870.

Soci, C., Hersbach, H., Simmons, A., Poli, P., Bell, B., Berrisford, P., Horányi, A., Muñoz-Sabater, J., Nicolas, J., Radu, R., Schepers, D., Villaume, S., Haimberger, L., Woollen, J., Buontempo, C., Thépaut, J.-N., 2024. The era5 global reanalysis from 1940 to 2022. Quarterly Journal of the Royal Meteorological Society n/a (n/a).
URL https://rmets.onlinelibrary.wiley.com/doi/abs/10.1002/qj.4803

Thompson, D. R., Leifer, I., Bovensmann, H., Eastwood, M., Fladeland, M., Frankenberg, C., Gerilowski, K., Green, R. O., Kratwurst, S., Krings, T., Luna, B., Thorpe, A. K., 2015. Real-time remote detection and measurement for airborne imaging spectroscopy: a case study with methane. Atmospheric Measurement Techniques 8 (10), 4383–4397.
URL https://amt.copernicus.org/articles/8/4383/2015/

Thompson, D. R., Thorpe, A. K., Frankenberg, C., Green, R. O., Duren, R., Guanter, L., Hollstein, A., Middleton, E., Ong, L., Ungar, S., 2016. Space-based remote imaging spectroscopy of the aliso canyon ch4 superemitter. Geophysical Research Letters 43 (12), 6571–6578.
URL https://agupubs.onlinelibrary.wiley.com/doi/abs/10.1002/2016GL069079

Thorpe, A. K., Frankenberg, C., Roberts, D. A., 2014. Retrieval techniques for airborne imaging of methane concentrations using high spatial and moderate spectral resolution: application to aviris. Atmospheric Measurement Techniques 7 (2), 491–506.
URL https://amt.copernicus.org/articles/7/491/2014/

Thorpe, A. K., Green, R. O., Thompson, D. R., Brodrick, P. G., Chapman, J. W., Elder, C. D., Irakulis-Loitxate, I., Cusworth, D. H., Ayasse, A. K., Duren, R. M., Frankenberg, C., Guanter, L., Worden, J. R., Dennison, P. E., Roberts, D. A., Chadwick, K. D., Eastwood, M. L., Fahlen, J. E., Miller, C. E., 2023. Attribution of individual methane and carbon dioxide emission sources using EMIT observations from space. Science Advances 9 (46), eadh2391.
URL https://www.science.org/doi/abs/10.1126/sciadv.adh2391

Varon, D. J., Jacob, D. J., Jervis, D., McKeever, J., 2020. Quantifying Time-Averaged Methane Emissions from Individual Coal Mine Vents with GHGSat-D Satellite Observations. Environmental Science & Technology 54 (16), 10246–10253, pMID: 32672947.
URL https://doi.org/10.1021/acs.est.0c01213

Varon, D. J., Jacob, D. J., McKeever, J., Jervis, D., Durak, B. O. A., Xia, Y., Huang, Y., 2018. Quantifying methane point sources from fine-scale satellite observations of atmospheric methane plumes. Atmospheric Measurement Techniques 11 (10), 5673–5686.
URL https://amt.copernicus.org/articles/11/5673/2018/

Varon, D. J., Jervis, D., McKeever, J., Spence, I., Gains, D., Jacob, D. J., 2021. High-frequency monitoring of anomalous methane point sources with multispectral sentinel-2 satellite observations. Atmospheric Measurement Techniques 14 (4), 2771–2785.
URL https://amt.copernicus.org/articles/14/2771/2021/

Varon, D. J., McKeever, J., Jervis, D., Maasakkers, J. D., Pandey, S., Houweling, S., Aben, I., Scarpelli, T., Jacob, D. J., 2019. Satellite discovery of anomalously large methane point sources from oil/gas production. Geophysical Research Letters 46 (22), 13507–13516.
URL https://agupubs.onlinelibrary.wiley.com/doi/abs/10.1029/2019GL083798

Wang, H., Fan, X., Jian, H., Yan, F., 2024. Exploiting the matched filter to improve the detection of methane plumes with sentinel-2 data. Remote Sensing 16 (6).
URL https://www.mdpi.com/2072-4292/16/6/1023